



CHALMERS
UNIVERSITY OF TECHNOLOGY

Delocalization Enhances Conductivity at High Doping Concentrations

Downloaded from: <https://research.chalmers.se>, 2022-07-02 09:28 UTC

Citation for the original published paper (version of record):

Derewjanko, D., Scheunemann, D., Järsvall, E. et al (2022). Delocalization Enhances Conductivity at High Doping Concentrations. *Advanced Functional Materials*, In Press.
<http://dx.doi.org/10.1002/adfm.202112262>

N.B. When citing this work, cite the original published paper.

Delocalization Enhances Conductivity at High Doping Concentrations


Dennis Derewjanko, Dorothea Scheunemann, Emmy Järsvall, Anna I. Hofmann, Christian Müller,* and Martijn Kemerink*

Many applications of organic semiconductors require high electrical conductivities and hence high doping levels. Therefore, it is indispensable for effective material design to have an accurate understanding of the underlying transport mechanisms in this regime. In this study, own and literature experimental data that reveal a power-law relation between the conductivity and charge density of strongly p-doped conjugated polymers are combined. This behavior cannot consistently be described with conventional models for charge transport in energetically disordered materials. Here, it is shown that the observations can be explained in terms of a variable range hopping model with an energy-dependent localization length. A tight-binding model is used to quantitatively estimate of the energy-dependent localization length, which is used in an analytical variable range hopping model. In the limit of low charge densities, the model reproduces the well-known Mott variable range hopping behavior, while for high charge densities, the experimentally observed superlinear increase in conductivity with charge density is reproduced. The latter behavior occurs when the Fermi level reaches partially delocalized states. This insight can be anticipated to lead to new strategies to increase the conductivity of organic semiconductors.

1. Introduction

Devices based on organic semiconductors hold the promise to be very flexible, scalable on large areas, light-weight, and cost-effective to produce.^[1–3] In fact, several applications like organic

D. Derewjanko, D. Scheunemann, M. Kemerink
Centre for Advanced Materials
Heidelberg University
Im Neuenheimer Feld 225, 69120 Heidelberg, Germany
E-mail: martijn.kemerink@cam.uni-heidelberg.de
E. Järsvall, A. I. Hofmann, C. Müller
Department of Chemistry and Chemical Engineering
Chalmers University of Technology
41296, Gothenburg, Sweden
E-mail: christian.muller@chalmers.se

 The ORCID identification number(s) for the author(s) of this article can be found under <https://doi.org/10.1002/adfm.202112262>.

© 2022 The Authors. Advanced Functional Materials published by Wiley-VCH GmbH. This is an open access article under the terms of the Creative Commons Attribution-NonCommercial License, which permits use, distribution and reproduction in any medium, provided the original work is properly cited and is not used for commercial purposes.

DOI: 10.1002/adfm.202112262

light emitting diode displays and organic solar cells have reached the market place, whereas others like organic thermoelectric generators are still under development.^[4,5] In all cases, the optimization of the involved active materials is a topic of intense research since many of the relevant figures of merit still lag behind their inorganic counterparts,^[4,5] forming a bottleneck for commercial relevance. Even now, doped polymers find interesting niche applications that inorganic materials can hardly fill. In virtually all cases, a specific concern is the limited electrical conductivity of the involved organic semiconductors,^[6–21] even at the currently highest available doping concentrations. In comparison to inorganic semiconductors, the physics behind doping of organic semiconductors appears considerably more intricate.^[22] For example, at high doping concentrations the steric properties and even the orientation of the dopant molecule affect the probability of charge

transfer and the overall conductivity.^[6,23,24] A further complication is that the doping changes the energetic landscape as seen by the moving charge carriers, which is commonly accounted for as a modification of the density of states.^[25–27] Concomitantly, charge transport in doped organic semiconductors is not yet fully understood, as evidenced by the absence of a universal, physics-based, as opposed to phenomenological, quantitative model. In order to be able to purposefully design optimal high-conductivity organic materials for their respective applications, that is, to make quantitative predictions, it is indispensable to have a precise knowledge of the underlying transport mechanisms at high charge carrier concentrations.

In this work, we compare a wide range of literature values as well as own data for the electrical conductivity σ and charge density n of a variety of p-doped conjugated polymers at high doping concentrations and observe a power-law,

$$\sigma \propto n^\gamma \quad (1)$$

with γ an exponent that typically lies in the range 2 to 5. This behavior is not predicted by conventional models for doped organic semiconductors as further detailed below. The purpose of the current work is to propose a minimal model to describe the carrier density dependence of the conductivity at all charge

carrier concentrations. Before proposing our solution, we will briefly review some previous studies.

Tanase et al. investigated poly(p-phenylene vinylene) (PPV) and poly(3-hexylthiophene) (P3HT) based hole-only diodes and field effect transistors and used the percolation model of Vissenberg and Matters (VM) to describe the data.^[28] Specifically, the VM model describes the charge density n dependency of the conductivity for an exponential density of states (DOS) as

$$\sigma \propto n^{T_0/T} \quad (2)$$

with T_0 the characteristic temperature. Good agreement of the experimental data and the model with characteristic temperatures of $T_0 = 425$ K for P3HT and $T_0 = 540$ K for a PPV derivative was found in the low- to intermediate density regime. However, an exponential DOS tail is not compatible with common observations of intrinsic organic semiconductors like a finite mobility value at low carrier density and the characteristic temperature dependence of the mobility^[29] $\mu \propto \exp(-(T_0/T)^2)$. The success of the VM model to describe field effect transistor data can be attributed to the additional dipolar energetic disorder at the interface between the organic and the gate dielectric that gives rise to an exponential tail below an otherwise Gaussian DOS.^[30,31]

Interestingly, it was shown by Bässler and coworkers that exponential DOS tails also arise as a consequence of doping due to the long-range Coulomb interaction with ionized dopants.^[25,26] When the resulting DOS is integrated in an analytical variable range hopping model, convincing agreement with both kinetic Monte Carlo simulations as well as experiments is found for low and intermediate doping concentrations.^[27] Particularly, this model could explain the quasi-universal power law relation $S \propto \sigma^{-1/4}$ between Seebeck coefficient S and conductivity that

is commonly observed.^[32,33] The universality of this behavior is directly related to the fact that the slope of the doping-induced exponential tail depends predominantly on the dielectric constant ϵ_r and the distance between the localized sites, that is the inter-site distance $a_{NN} \propto N_i^{-1/3}$ with N_i the total density of localized states, and not on the charge carrier density. Since ϵ_r and N_i vary only little between different materials, the slope of the induced tail therefore hardly depends on the investigated material. Hence, the observed strong variation in the exponent γ in Equation (1) is at odds with a picture where a doping-induced exponential tail explains the observed quasi-universal power law behavior at high charge carrier densities of the shape of Equation (2). The experimental data summarized in Figure 1 below show that to do so, T_0 would, at room temperature, have to vary between 600 and 1500 K, which is difficult to reconcile with the constant slope in the power law between S and σ .

A recent paper by Gregory et al. uses the overlap of Coulomb potentials of neighboring ionized dopants to define a dopant concentration c_D dependent activation barrier $W_H(c_D)$ for transport.^[34] Before, the same idea was explored by Arkhipov et al., c.f. Equation (1) in ref. [35] where the latter used the term trapping instead of localization for the same effect. We note that associating the barrier height W_H with a degree of localization suggests that the charge carrier is only confined by the dopant Coulomb potentials, which is not generally correct for organic semiconductors that show hopping transport at all dopant concentrations. The expression for W_H is then used to modify a model from Kang and Snyder by introducing $W_H(c_D)$ as an Arrhenius term into a transport function $\sigma_E(E-E_t)$ where E_t is the so-called transport edge.^[36] The resulting semi-localized transport (SLoT) model overcomes several issues of the original Kang-Snyder model, including the need for unrealistic positions of the Fermi energy to fit experimental data.^[37] In passing, we note that the function $\sigma_E(E-E_t)$ that was used as a starting point by Kang-Snyder can provide accurate but entirely phenomenological fits to conductivity distribution functions that are derived from the Schmechel model for hopping transport.^[38,39] The SLoT model can indeed provide convincing fits to experimental Seebeck coefficient versus conductivity data for different polymers and a large conductivity range. Unfortunately, the model requires a dielectric constant of $\epsilon_r \approx 16$ which is too high considering that values of about $\epsilon_r \approx 3 - 4$ are observed for many conjugated polymers^[40-42] and still larger than $\epsilon_r \approx 8 - 9$ of polymers with highly polarizable side chains.^[43]

Here, we show that a simple semi-analytical model based on the Gaussian disorder model (GDM) in combination with an analytical expression for the energy dependent localization length $\alpha^{-1}(E)$ can quantitatively describe the experimentally observed power-law trends of the conductivity with charge density at high doping concentrations using physically meaningful parameters. The function $\alpha^{-1}(E)$ is determined on the basis of numerically exact solutions of a 3D tight binding model. At low doping concentrations, the functional shape of the well-known Mott variable range hopping model is recovered.

2. Experimental Results

The conductivity versus charge density data for a wide range of materials are assembled in Figure 1, including polythiophenes

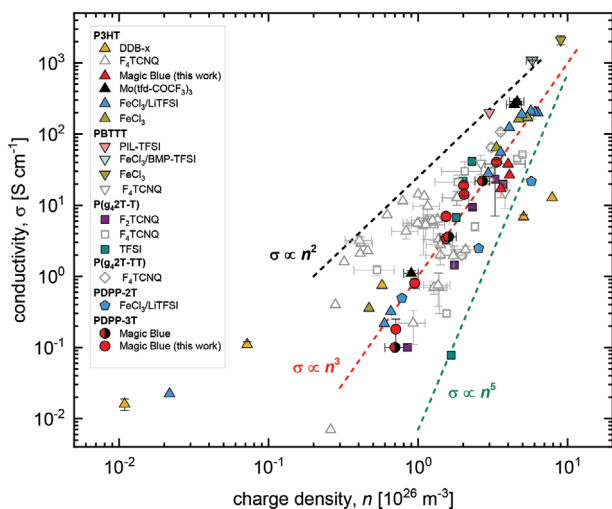


Figure 1. Collection of experimental data of conductivity σ versus charge density n for p-doped conjugated polymers measured as part of this work (red) or extracted from refs. [6–12,15–18,44,45] (all data are unaligned polymers). The dashed lines are power laws of varying slopes that were added to guide the eye. P3HT, PBTTT, P(g_4 2T-T), P(g_4 2T-TT), PDPP-2T and PDPP-3T are doped with F_2 TCNQ, F_4 TCNQ, TFSI, a polymeric ionic liquid (PIL)-TFSI complex, $FeCl_3$, $FeCl_3$ /BMP-TFSI, $FeCl_3$ /LiTFSI, $Mo(tfd-COCF_3)_3$, dodecaborane (DDB) based dopants or Magic Blue (see Figure S2, Supporting Information for chemical structures and Table S3, Supporting Information for details about how the carrier density was estimated in each case).

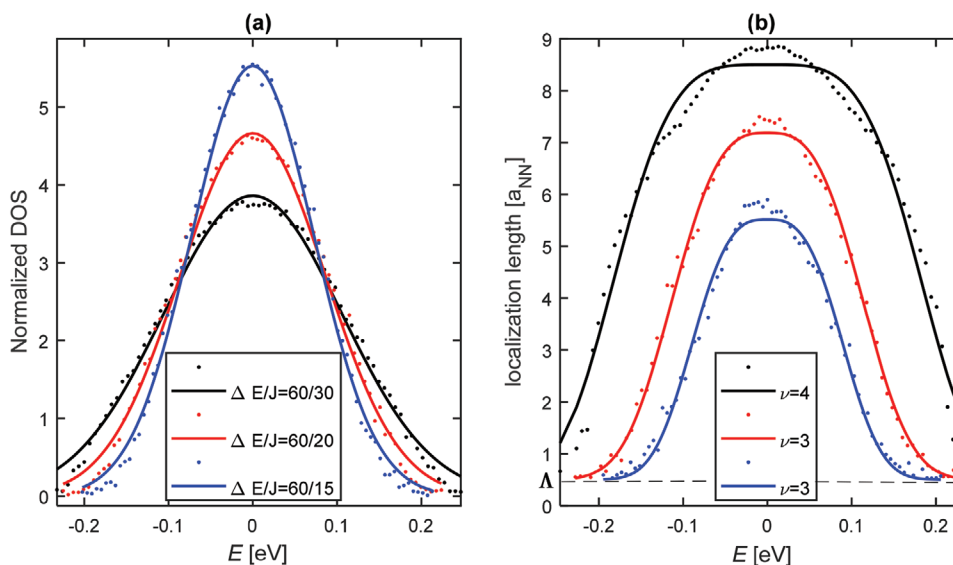


Figure 2. a) Normalized density of states for different ratios between diagonal disorder ΔE and transfer integral J (both in meV). b) Corresponding localization lengths. Symbols and lines are numerical results and fits with Equations (7) and (8), respectively, where ν is a parameter from Equation (8). In the calculations, we used $\Lambda = \lambda/a_{NN} = 0.5$.

and bithiophene-thienothiophene copolymers with alkyl as well as oligoether side chains as well as diketopyrrolopyrrole (DPP) based copolymers. At high charge density, the vast majority of data points are confined by the black and green lines that are power laws (Equation (1)) with slopes 2 and 5, respectively. In addition, individual data sets mostly follow power law trends. Similar behavior was for example observed for P3HT thin films or in organic transistors in refs. [10,16,35] where it was either interpreted in terms of Coulomb interactions or not commented upon. In the following, we shall demonstrate that the observed behavior, that is, a power law functional dependence with variable slope, follows naturally when accounting for an energy dependent localization length in a variable range hopping model.

3. Theoretical Model

Our first aim is to obtain an expression for the energy-dependent localization length. We therefore start with a non-interacting Anderson-like tight binding Hamiltonian on a regular lattice

$$H = \sum_i \varepsilon_i a_i^\dagger a_i + \sum_{\langle i,j \rangle} \overbrace{h\nu_0 \exp\left(-\frac{2a_{NN}}{\lambda}\right)}^J (a_i^\dagger a_j + h.c.) \quad (3)$$

where a_i^\dagger and a_i are the respective creation and annihilation operators of charges at lattice site i of a lattice with inter-site distance (intermolecular distance) a_{NN} . The expression $\langle i, j \rangle$ denotes the summation over nearest neighbor sites and h.c. means Hermitian conjugated. The on-site energies ε_i are randomly drawn from a Gaussian distribution with width or on-site-disorder energy ΔE . For simplicity, the transfer integral J is taken to be equal for every site and to fall off exponentially^[46] with distance with decay length λ , which is the localization

length of the local Wannier orbital function of the lattice sites. The energy $h\nu_0$ can be understood as the value at full overlap of two Wannier orbitals and shifts the transfer integral to reasonable energy values. In general, the transfer integral can be calculated as the transition element

$$J_{\tau\tau'}(r_i, r_j) = \langle \omega_{\tau'}(r_j) | H | \omega_{\tau}(r_i) \rangle \quad (4)$$

between the orthonormal Wannier orbitals $\omega_{\tau}(r_i)$, which are calculated to be maximally localized or maximally molecular-like, where τ maybe some quantum number as, for example, spin. At this point, we want to emphasize that we chose to work on a regular lattice. Since we are explicitly interested in the energetics of the localization length, this choice allows us to disentangle possible spatial correlations from energetic correlations of the localization length. This is also the reason why counter ions are not considered since the corresponding Coulomb potential introduces long-range spatial correlations.

Given this Hamiltonian, one can now numerically diagonalize and extract the eigenenergies and eigenstates of the Hamiltonian. To do so, we used a self-written MatLab program that works on a 3D box of typically $N_i = 20 \times 20 \times 20 = 8000$ sites with periodic boundary conditions. Averages were taken over 5 random realizations to obtain sufficient numerical accuracy. The DOS can now be obtained by dividing the relevant energy interval, defined by the minimal and maximal calculated eigenenergies, into bins of appropriate width and counting the eigenvalues in every bin. As seen in **Figure 2a**, this provides a close to Gaussian-shaped DOS. In order to maintain consistency with the original GDM, we fitted a Gaussian shape to the DOS to obtain the disorder σ_{DOS} . We note that the latter is not simply equal to ΔE . Instead, we observe that

$$\sigma_{DOS} \approx \Delta E + J \quad (5)$$

which is a useful relation to set the parameters to realistic values.

Denoting the components of the eigenstate vectors as V_i we now define the discrete inverse participation ratio (IPR)^[47] as

$$\text{IPR} = \frac{1}{\sum_i |V_i|^4} \quad (6)$$

The IPR equals unity for a state that is localized to one lattice site n , as $V_i = \delta_{in}$ and equals the total number of lattice sites N_i for a completely delocalized state $V_i = \frac{1}{\sqrt{N_i}}$ for all sites i . By a simple dimensional consideration one can now define an estimate of the localization length by taking the third root of the IPR^[48] and multiplying with a_{NN} . However, the distance to the next lattice site is not the minimal localization length in the system. Instead, the physical limit of localization is rather set by the characteristic decay length λ of the local Wannier functions. We therefore arrive at the approximated expression for the localization length

$$\alpha^{-1}(E) = \sqrt[3]{\text{IPR}(E)} - 1 + \lambda / a_{\text{NN}} \quad (7)$$

Note that in our discrete model distances are normalized to a_{NN} . After averaging the localization lengths over each energy bin interval, we can plot the energy dependent localization length, c.f. Figure 2b and fit a suitable function. We empirically find a suitable fit with

$$\alpha^{-1}(E) = \alpha_0 \exp\left(-\frac{|E|^v}{\eta}\right) + \lambda \quad (8)$$

where $v = 2, 3, 4$, depending on the ratio $\Delta E/J$. For $\Delta E \gg J$ the most suitable value is $v = 2$ and for $J \rightarrow \Delta E$ we find $v = 4$. For intermediate values of $\Delta E/J$, that is, the most realistic ratios between on-site energy disorder and transfer integral, $v = 3$ gave the best results. For this empirical model it is sufficient to take the fitting parameter v integer valued. Comparing the DOS in Figure 2a and the localization length in Figure 2b, one observes a clear correlation between the two, with larger values of $\Delta E/J$ leading to stronger localized states, especially in the DOS tails, whereas the width of the DOS approximately equals the width of the localization length distribution.

It should be kept in mind that Figure 2 shows averaged distributions, and that the localization length of a particular state rather depends on its local DOS. In other words, not all states at a given energy have the same IPR and localization length. Nevertheless, we concentrate on the macroscopic behavior and therefore assume a scale invariant DOS, which means that the local DOS is the same as the macroscopic DOS, or in other words, we do not account for spatial correlations in the energy landscape.

Having extracted the localization length from the numerical calculation, we now use the value in a Mott–Martens-like variable-range-hopping (VRH) model.^[49,50] For that, we define a transition probability

$$p(E^*) = \exp\left(-R^* (\alpha(E_F) + \alpha(E^*)) - \frac{E^* - E_F}{k_B T}\right) \quad (9)$$

that is determined by a critical hop from the Fermi level E_F to some, yet to be determined, transport energy E^* and over a critical hopping distance R^* , at temperature T . This approximation holds provided that the transition probability has a sharp maximum for some energy E^* , which turns out to be the case here as can be seen by plotting $R^*(E^*)$.^[51] Note the difference to previous models: instead of the common term $2R^*\alpha$ in the first exponential function in the transition probability with a constant inverse localization length α , we now split the exponential function into two factors. The first factor $\exp(-R^*\alpha(E_F))$ is the contribution to the tunneling term of the starting site at the Fermi level with inverse localization length $\alpha(E_F)$, the second factor $\exp(-R^*\alpha(E^*))$ is the same for the final site at energy E^* . Since we have two unknown variables here, we need another condition, which we get from the common percolation argument. The critical average number of bonds per lattice site to get a connected transport path provides the critical hopping distance as a function of the final hopping energy E^* ^[37]

$$B_c = \frac{4}{3} \pi R^{*3} \int_{E_F}^{E^*} g(\epsilon) d\epsilon \quad (10)$$

for isotropic and homogeneous media, where numerical simulations determine $B_c \cong 2.8$.^[37] We now get the transport energy E_{tr} by finding the maximum of the transition probability by differentiation. The mobility can now be defined as $\mu = \mu_0 p(E^*)/c$, where c is the charge carrier concentration (fraction of lattice sites occupied by charges) and $\mu_0 = B \frac{q a_{\text{NN}}^2 v_0}{\sigma_{\text{DOS}}}$, where $B = 0.47$ for a regular SC lattice.^[52] From there we obtain the conductivity by $\sigma = \mu q N_i c$, where q is the elementary charge and $N_i = a_{\text{NN}}^{-3}$ is the total site density. To rewrite the formulas in terms of charge density n , one has to use $n = N_i c$. For the latter comparison, Equations (9)–(10) with $\alpha(E_F) = \alpha(E^*) = \alpha$ can be used to calculate the conductivity according to the conventional Mott–Martens model.^[49,50]

4. Results and Discussion

From the data in Figure 1, we chose a representative set of different organic semiconductors with different dopants and fitted our model to the data; the result is shown in Figure 3. Despite the simplicity of the model, it fits the experimental data well. At low density, the model converges to the conventional Mott–Martens model, as shown by the green line in panel a, which, for the shown densities, gives rise to a slightly super-linear behavior due to state filling effects. For calculation of the Mott–Martens curve, we used the same parameters as in our model, set $\alpha = (\alpha(E_F) + \alpha(E^*))/2$ for some low charge density and normalized the curve to a point at low charge density; the result is independent of the exact density used. In the full model, a power law regime sets in at around 10^{26} m^{-3} that subsequently saturates at very high charge carrier concentrations ($\approx 10^{27} \text{ m}^{-3}$), that is, near half filling of the DOS.

The parameters used in the model calculations in Figure 3 are summarized in Table 1. The diagonal disorder energies, transfer integrals with their corresponding decay lengths take physically reasonable values in view of previous works.^[46,53,54] One interesting difference with previous incarnations of the

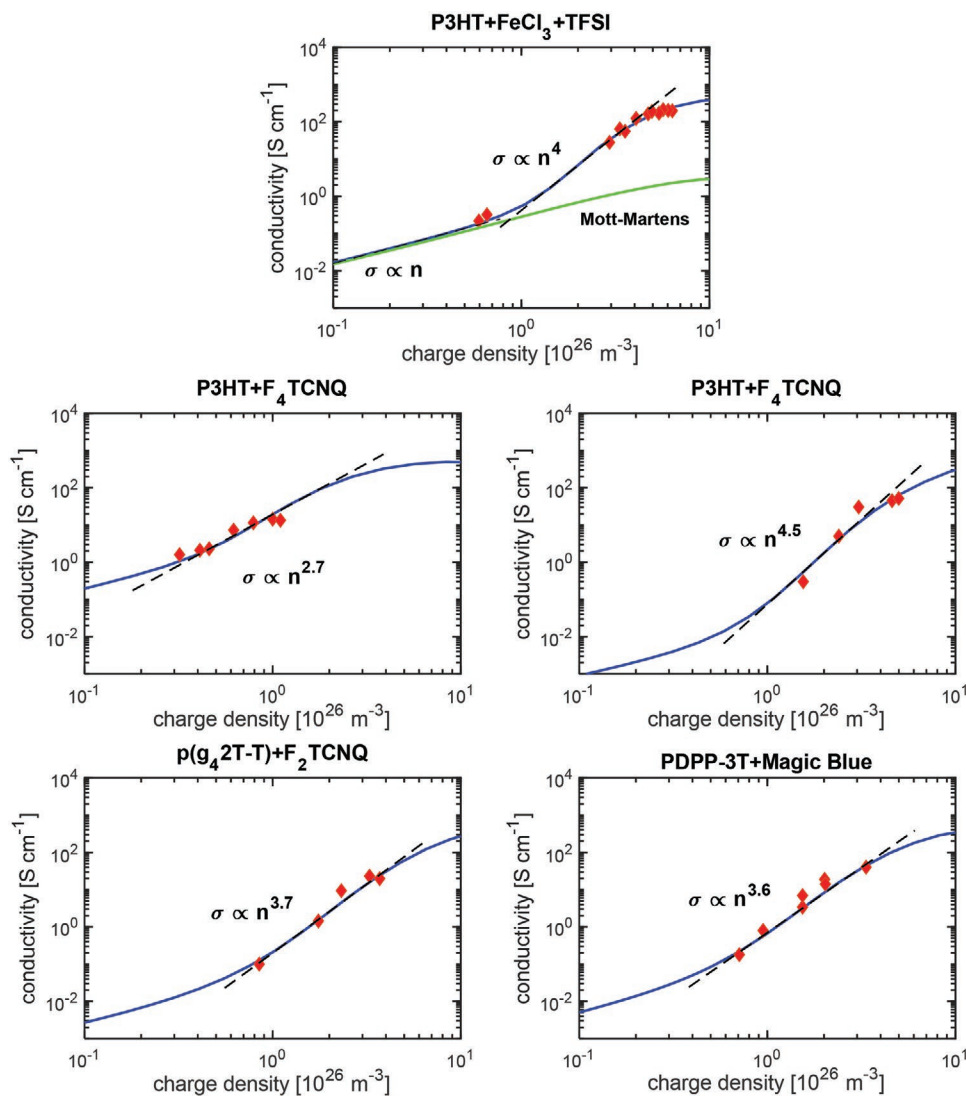


Figure 3. Conductivity versus charge density $\sigma(n)$ for a representative subset of materials from Figure 1. Symbols are the experimental data, solid lines are fit to the model described in the text with the parameters given in Table 1, dashed lines indicate power laws of given exponent. The first panel shows also the Mott–Martens model (solid green line) for comparison.

Table 1. Fit parameters used in the simulations of Figure 3. Since the error calculation sometimes resulted in poor error estimates (see Supporting Information for details), manual estimates for the errors are given as $\Delta(\Delta E) = 10$ meV, $\Delta a_{\text{NN}} = 0.05$ nm, $\frac{\Delta \lambda}{a_{\text{NN}}} = 0.1$, $\Delta J = 10$ meV.

	P(g_4 2T-T) + F4TCNQ	PDPP-3T + Magic Blue	
a_{NN} [nm]	0.44	0.76	
λ [a_{NN}]	0.35	0.4	
ΔE [meV]	50	60	
J [meV]	20.5	13.9	
	P3HT + FeCl ₃ + TFSI	P(g_4 2T-T) + F ₂ TCNQ	P3HT + F ₄ TCNQ
a_{NN} [nm]	0.73	0.67	0.82
λ [a_{NN}]	0.5	0.35	0.8
ΔE [meV]	60	60	60
J [meV]	15.2	13.6	17

GDM are the fitted values of a_{NN} . While previous GDM fits to experiments led to values in the range 1–2 nm, that is significantly above an intermolecular distance, a_{NN} here does take the value of an intermolecular distance (≈ 0.4 – 0.8 nm), which is consistent with the assumptions of the tight binding model.^[33,55] A further discussion of the fitting procedure and error bar estimation can be found in the Supporting Information.

Figure 4 rationalizes the changes in slope observed in Figures 1 and 3. One can divide the localization length curve (panel a) into three regimes. In regime I, the charge carrier concentration is so low that the Fermi level (panel b) is located in the energy interval in which the localization length is about constant. Further, the transport energy is constant in this regime. Here, we can define a constant effective inverse localization length $2^* \alpha_{\text{eff}} = \alpha(E_{\text{F}}) + \alpha(E_{\text{tr}})$ and we are therefore in the regime of the standard Mott–Martens model and do not observe a significant deviation from the latter model.

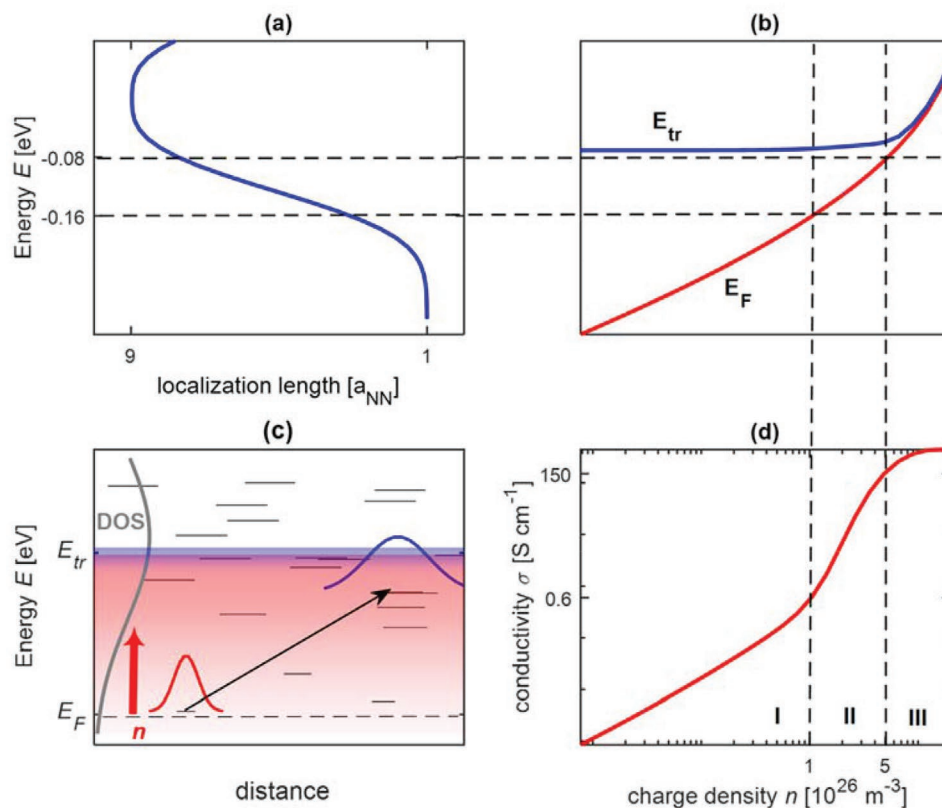


Figure 4. Illustration of the reason for the change of slopes in the $\sigma(n)$ double-log plots Figures 1 and 3. Panel (a) shows the dependence of the localization length versus site energy, which, using the charge density dependence of the Fermi and Transport energies in panel (b) can be converted to the conductivity versus density relation in panel (d). Panel (c) illustrates the hopping process between two sites with different energies and localization length, indicated by different lengths of lines and the schematic (colored) wavefunctions. Red and blue color gradients indicate the change of Fermi level and transport energy with charge density n (red arrow). The indicated regions I–III in panel (d) divide the graph into the respective regimes of linear, power-law, and saturation behavior of the conductivity.

This changes when we further increase the charge density. At some point, the state filling has advanced to such an extent, that the Fermi level enters regime II where the states become more delocalized and we obtain a new contribution to the slope since $\frac{d\alpha}{dn}(E_F(n)) > 0$. The transport energy remains close to constant in this regime, which explains the observed strongly superlinear increase of the conductivity with carrier density. More precisely, in the middle of regime II one can assume the slopes in the graphs of $E(\log(n))$ and $\alpha(E)$, c.f. Figure 2b, to be about constant and slowly changing. Therefore we can locally assume $\alpha = \text{const.} \times E$, $E_F = \text{const.} \times \log(n)$, leading directly to $\alpha(E_F) = \text{const.} \times \log(n)$. Putting this into the transition probability we get $p(E_{tr}) \propto \exp(-R^* \times \text{const.} \times \log(n) - \frac{\text{const.}}{k_B T} \log(n)) = n^{\text{const.}}$ where the exponent is locally constant and slowly changing in the middle of regime II. The prefactors and the local slopes of the functions of E_F in the exponential function therefore determine the slope of $\log(\sigma)$ vs. $\log(n)$.

After this steeper rise in conductivity, one enters a regime where the Fermi level approaches the transport energy and where the localization lengths saturate. We therefore see a saturation in the conductivity. For even larger densities, roughly beyond relative occupations of 0.1, the present VRH model is

likely no longer sufficient, and other physical effects like band-like transport or sign inversions of the Seebeck coefficient might be expected to occur.^[56] This also may be the reason why in Figure 1 all curves seem to saturate at a conductivity of about $\sigma \approx 10^3 \text{ S cm}^{-1}$.

For practical applications and materials design, it is interesting to investigate which parameters determine the slope in the power-law regime of the conductivity. By changing parameters and by studying the functional dependence of the involved parameters, we find that the relative decay length $\Lambda = \lambda/a_{\text{NN}}$ is the most critical parameter that determines the slope. To explain this, we look at the Fermi part of the tunneling term in the transition probability $p \propto \exp(-R/(\tilde{\alpha}(E_F) + \Lambda))$, where we separate the offset from the localization length: $(\tilde{\alpha}(E_F) + \Lambda)^{-1} = \alpha(E_F)$. Considering the change of this term with charge density we arrive at

$$\frac{d}{dn} (\tilde{\alpha}(E_F(n) + \Lambda))^{-1} = - \frac{d\tilde{\alpha}/dn}{(\tilde{\alpha}(E_F(n) + \Lambda)^2)} \quad (11)$$

which implies a suppression of the contribution to the slope for larger Λ . For lower Λ it is harder for the charge carriers to delocalize, so that the conductivity is lower and the threshold for delocalization to occur is reached at higher doping levels.

However, once the threshold is reached this process happens quite fast with rising doping concentration. On the other hand, for higher Λ , delocalization is easier and happens more smoothly. Since Λ seems to be a crucial quantity in our model, it may be possible to extract information about the electronic coupling of the OSC from conductivity measurements at high doping concentrations.

In addition, looking at the general shape of the localization length curve Figure 2b, a shorter rise in $\alpha^{-1}(E)$ therefore usually means a steeper and narrower region of superlinear growth. As discussed previously, the shape of this curve is closely related to that of the DOS, so one may engineer the localization properties by controlling the DOS. In general, the width of the DOS gives the approximate width of the localization distribution. What is more important is the scaling of the localization length distribution, which is very sensitive to changes in the transfer integral, meaning that larger transfer integrals result in an increase in localization length, while being less sensitive to changes in on-site-energetical disorder, where less disorder improves delocalization. This effect is independent of any additional changes in overlap that would most likely further enhance this trend.

As a practical illustration of the preceding discussion, one may consider the experimentally well-documented effects of chain stiffening and increasing conjugation length upon doping.^[6,57–59] Although these effects cannot be accounted for explicitly in the present model, they are expected to improve the delocalization, both directly, via increased transfer integrals due to a larger overlap between neighboring sites, and indirectly, by a reduction of the on-site-energy disorder. Likewise, a high degree of regioregularity or rigidity of the molecular backbone will also enhance delocalization.

Also, since the transport energy is largely constant, it is beneficial to have a large DOS at the Fermi level, which for example has been argued to be achievable by molecules with a large dielectric constant.^[25,60] Finally, as a design rule, the conductivity at constant charge carrier concentration $c = n/N_i$ can be improved by decreasing the intermolecular distance a_{NN} . Although this would (quadratically) decrease the mobility prefactor μ_0 , the overall conductivity prefactor $q\mu_0n$ would (linearly) increase due to the (cubic) increase of N_i and, at constant c , n with a_{NN} . Probably more importantly, the transfer integral J , Equation (3), will, at approximately constant localization length, increase exponentially with decreasing a_{NN} . Experimentally, this could be achieved in polymers with shorter side chains or the use of smaller, better intercalating dopant ions.^[15,61] Evidently, the value of $\Lambda = \lambda/a_{NN}$, which determines the orbital overlap of neighboring molecules should in general be as large as possible.

5. Conclusion

We assembled a large number of experimental data of conductivity versus charge density and observed a power-law trend with exponents in the range 2 to 5 for charge densities above $\approx 10^{26} \text{ m}^{-3}$. To explain this, we developed a semi-analytical model to include the energy dependence of the localization length into a Mott-like transport model. The energy dependence of the localization length was estimated from the inverse participation ratio

of the eigenvectors of a tight binding Hamiltonian. We find that we reproduce Mott-like behavior of the conductivity for low to intermediate charge carrier concentrations, while describing the experimentally observed power-law trend for higher charge carrier densities. This behavior could be explained with the charge delocalization at the Fermi level. Finally, we find convincing agreement with diverse experimental data for different conjugated polymers p-doped with a range of different dopants with meaningful physical parameters. Our model reveals the importance of considering the energy dependence of the localization parameters relevant for charge transport. Further, the developed model may provide details about the electronic coupling of the doped OSC from studying the conductivity at high doping levels.

6. Experimental Section

Materials: P3HT (number-average molecular weight $M_n = 24 \text{ kg mol}^{-1}$, polydispersity index = 2.4, regioregularity $\approx 88\%$) was purchased from Solaris Chem and Poly[[2,5-bis(2-hexyldecyl)-2,3,5,6-tetrahydro-3,6-dioxopyrrolo[3,4-c]pyrrole-1,4-diyl]-*alt*-[3',3''-dimethyl-2,2':5',2''-terthiophene]-5,5''-diyl] (PDPP-3T; $M_n = 83 \text{ kg mol}^{-1}$, polydispersity index = 2.1) was purchased from Solarmer [(4-BrC₆H₄)₃N]SbCl₆ (Magic Blue) and anhydrous acetonitrile (AcN) were purchased from Sigma Aldrich. Chlorobenzene (CB) and chloroform (CHCl₃) were obtained from VWR. All polymers, solvents and dopants were used as received. Full chemical structures of polymers and dopants used in this work are shown in Figure S2, Supporting Information.

Sample Preparation: P3HT and PDPP-3T were dissolved in CB (10 g L⁻¹ and 8.5 g L⁻¹) and the solutions were spin cast onto CaF₂ substrates yielding a film thickness of ≈ 50 and 100 nm, respectively. The polymer films coated on CaF₂ were sequentially doped with a solution of Magic Blue in AcN (0.15–0.5 g L⁻¹) by immersing the films into solutions with different concentrations during 30 s for PDPP-3T and 60 s for P3HT.

UV–Vis Absorption Spectroscopy: UV–vis–NIR spectra were recorded with a PerkinElmer Lambda 1050 spectrophotometer.

Electrical Characterization: The electrical resistivity was measured with a four-point probe setup from Jandel Engineering (cylindrical probe head, RM3000) using collinear tungsten carbide electrodes with equidistant spacing of 1 mm that were held down with a constant weight of 60 g. The electrical conductivity (σ) was then calculated according to $\sigma^{-1} = (V/I) \cdot kt$ where V is the voltage, I the current, $k = 4.53$ a geometrical correction factor, and t the film thickness.

Determination of Oxidation Level: To estimate the charge-carrier density N_v of the molecularly doped polymers the Beer–Lambert law $A_{\text{polaron}} = \epsilon_{\text{polaron}} \cdot t \cdot N_v$ was used, where A_{polaron} is the absorbance of the first sub-bandgap polaronic absorption peak and $\epsilon_{\text{polaron}}$ the molar attenuation coefficient with a value of $\epsilon_{\text{polaron}} = 4.1 \cdot 10^3 \text{ m}^2 \text{ mol}^{-1}$ at 800 nm in case of P3HT and $\epsilon_{\text{polaron}} = 6.0 \cdot 10^3 \text{ m}^2 \text{ mol}^{-1}$ at 1200 nm in case of PDPP-3T (see Figure S4, Supporting Information for representative UV–vis–NIR absorbance spectrum of doped PDPP-3T), obtained through a combination of spectro-electrochemistry and chronoamperometry.^[12,18]

Supporting Information

Supporting Information is available from the Wiley Online Library or from the author.

Acknowledgements

This work was financially supported by the European Commission through the Marie Skłodowska-Curie projects HORATES (GA-955837) and HyThermEl (GA-799477). M.K. thanks the Carl Zeiss Foundation

for financial support. C.M. acknowledges financial support from the Swedish Research Council (grant no. 2018-03824) and the Knut and Alice Wallenberg Foundation through a Wallenberg Academy Fellowship Prolongation grant.

Open access funding enabled and organized by Projekt DEAL.

Conflict of Interest

The authors declare no conflict of interest.

Data Availability Statement

The data that support the findings of this study are available from the corresponding author upon reasonable request.

Keywords

charge carrier delocalization, charge density, conductivity, doping, organic semiconductors

Received: December 1, 2021

Revised: January 21, 2022

Published online:

- [1] S. Forrest, *Nature* **2004**, 428, 911.
- [2] T. Someya, Y. Kato, T. Sekitani, S. Iba, Y. Noguchi, Y. Murase, H. Kawaguchi, T. Sakurai, *Proc. Natl. Acad. Sci. U. S. A.* **2005**, 102, 12321.
- [3] I. Manunza, A. Bonfiglio, *Biosens. Bioelectron.* **2007**, 22, 2775.
- [4] L. Tzounis, in *Advanced Thermoelectric Materials for Energy Harvesting Applications* (Ed: S. Memon), IntechOpen, London **2019**, p. 3.
- [5] D. Champier, *Energy Convers. Manage.* **2017**, 140, 167.
- [6] E. Lim, A. M. Glauddell, R. Miller, M. L. Chabiny, *Adv. Electron. Mater.* **2019**, 5, 1800915.
- [7] J. Hynynen, D. Kiefer, L. Yu, R. Kroon, R. Munir, A. Amassian, M. Kemerink, C. Müller, *Macromolecules* **2017**, 50, 8140.
- [8] J. Hynynen, D. Kiefer, C. Müller, *RSC Adv.* **2018**, 8, 1593.
- [9] T. J. Aubry, J. C. Axtell, V. M. Basile, K. J. Winchell, J. R. Lindemuth, T. M. Porter, J. Liu, A. N. Alexandrova, C. P. Kubiak, S. H. Tolbert, A. M. Spokoy, B. J. Schwartz, *Adv. Mater.* **2019**, 31, 1805647.
- [10] T. L. Murrey, M. A. Riley, G. Gonel, D. D. Antonio, L. Filardi, N. Shevchenko, M. Mascal, A. J. Moulé, *J. Phys. Chem. Lett.* **2021**, 12, 1284.
- [11] T. J. Aubry, K. J. Winchell, C. Z. Salamat, V. M. Basile, J. R. Lindemuth, J. M. Stauber, J. C. Axtell, R. M. Kubena, M. D. Phan, M. J. Bird, A. M. Spokoy, S. H. Tolbert, B. J. Schwartz, *Adv. Funct. Mater.* **2020**, 30, 2001800.
- [12] V. Untilova, J. Hynynen, A. I. Hofmann, D. Scheunemann, Y. Zhang, S. Barlow, M. Kemerink, S. R. Marder, L. Biniek, C. Müller, M. Brinkmann, *Macromolecules* **2020**, 53, 6314.
- [13] R. Kroon, D. Kiefer, D. Stegerer, L. Yu, M. Sommer, C. Müller, *Adv. Mater.* **2017**, 29, 1700930.
- [14] D. Kiefer, R. Kroon, A. I. Hofmann, H. Sun, X. Liu, A. Giovannitti, D. Stegerer, A. Cano, J. Hynynen, L. Yu, Y. Zhang, D. Nai, T. F. Harrelson, M. Sommer, A. J. Moulé, M. Kemerink, S. R. Marder, I. McCulloch, M. Fahlman, S. Fabiano, C. Müller, *Nat. Mater.* **2019**, 18, 149.
- [15] V. Vijayakumar, E. Zaborova, L. Biniek, H. Zeng, L. Herrmann, A. Carvalho, O. Boyron, N. Leclerc, M. Brinkmann, *ACS Appl. Mater. Interfaces* **2019**, 11, 4942.
- [16] E. M. Thomas, B. C. Popere, H. Fang, M. L. Chabiny, R. A. Segalman, *Chem. Mater.* **2018**, 30, 2965.
- [17] V. Vijayakumar, Y. Zhong, V. Untilova, M. Bahri, L. Herrmann, L. Biniek, N. Leclerc, M. Brinkmann, *Adv. Energy Mater.* **2019**, 9, 1900266.
- [18] A. I. Hofmann, R. Kroon, S. Zokaei, E. Järsvall, C. Malacrida, S. Ludwigs, T. Biskup, C. Müller, *Adv. Electron. Mater.* **2020**, 6, 2000249.
- [19] X. Fan, W. Nie, H. Tsai, N. Wang, H. Huang, Y. Cheng, R. Wen, L. Ma, F. Yan, Y. Xia, *Adv. Sci.* **2019**, 6, 1900813.
- [20] R. Sarabia-Riquelme, M. Shahi, J. W. Brill, M. C. Weisenberger, *ACS Appl. Polym. Mater.* **2019**, 1, 2157.
- [21] O. Bubnova, Z. U. Khan, H. Wang, S. Braun, D. R. Evans, M. Fabretto, P. Hojati-Talemi, D. Dagnelund, J.-B. Arlin, Y. H. Geerts, S. Desbief, D. W. Breiby, J. W. Andreasen, R. Lazzaroni, W. M. Chen, I. Zozoulenko, M. Fahlman, P. J. Murphy, M. Berggren, X. Crispin, *Nat. Mater.* **2014**, 13, 190.
- [22] T. A. Skotheim, R. L. Elsenbaumer, J. R. Reynolds, *Handbook of Conducting Polymers*, Marcel Dekker, New York **1998**.
- [23] D. di Nuzzo, C. Fontanesi, R. Jones, S. Allard, I. Dumsch, U. Scherf, E. von Hauff, S. Schumacher, E. da Como, *Nat. Commun.* **2015**, 6, 6460.
- [24] D. T. Duong, C. Wang, E. Antono, M. F. Toney, A. Salleo, *Org. Electron.* **2013**, 14, 1330.
- [25] M. Silver, L. Pautmeier, H. Bässler, *Solid State Commun.* **1989**, 72, 177.
- [26] V. I. Arkhipov, P. Heremans, E. v. Emelianova, H. Bässler, *Phys. Rev. B* **2005**, 71, 045214.
- [27] G. Zuo, H. Abdalla, M. Kemerink, *Phys. Rev. B* **2016**, 93, 235203.
- [28] C. Tanase, E. J. Meijer, P. W. M. Blom, D. M. Leeuw, *Phys. Rev. Lett.* **2003**, 91, 216601.
- [29] S. D. Baranovskii, H. Cordes, F. Hensel, G. Leising, *Phys. Rev. B* **2000**, 62, 7934.
- [30] T. Richards, M. Bird, H. Siringhaus, *J. Chem. Phys.* **2008**, 128, 234905.
- [31] W. S. C. Roelofs, S. G. J. Mathijssen, R. A. J. Janssen, D. M. de Leeuw, M. Kemerink, *Phys. Rev. B* **2012**, 85, 085202.
- [32] A. M. Glauddell, J. E. Cochran, S. N. Patel, M. L. Chabiny, *Adv. Energy Mater.* **2015**, 5, 1401072.
- [33] H. Abdalla, G. Zuo, M. Kemerink, *Phys. Rev. B* **2017**, 96, 241202.
- [34] S. A. Gregory, R. Hanus, A. Atassi, J. M. Rinehart, J. P. Wooding, A. K. Menon, M. D. Losego, G. J. Snyder, S. K. Yee, *Nat. Mater.* **2021**, 20, 1414.
- [35] V. I. Arkhipov, E. v. Emelianova, P. Heremans, H. Bässler, *Phys. Rev. B* **2005**, 72, 235202.
- [36] S. D. Kang, G. J. Snyder, *Nat. Mater.* **2017**, 16, 252.
- [37] G. Zuo, H. Abdalla, M. Kemerink, *Adv. Electron. Mater.* **2019**, 5, 1800821.
- [38] D. Scheunemann, M. Kemerink, in *Organic Flexible Electronics* (Eds: P. Cosseddu, M. Caironi), Elsevier, Amsterdam **2021**, pp. 165-197.
- [39] R. Schmechel, *J. Appl. Phys.* **2003**, 93, 4653.
- [40] K. Xu, H. Sun, T.-P. Ruoko, G. Wang, R. Kroon, N. B. Kolhe, Y. Puttisong, X. Liu, D. Fazzi, K. Shibata, C.-Y. Yang, N. Sun, G. Persson, A. B. Yankovich, E. Olsson, H. Yoshida, W. M. Chen, M. Fahlman, M. Kemerink, S. A. Jenekhe, C. Müller, M. Berggren, S. Fabiano, *Nat. Mater.* **2020**, 19, 738.
- [41] M. P. Hughes, K. D. Rosenthal, N. A. Ran, M. Seifrid, G. C. Bazan, T. Nguyen, *Adv. Funct. Mater.* **2018**, 28, 1801542.
- [42] J. Brebels, J. v. Manca, L. Lutsen, D. Vanderzande, W. Maes, *J. Mater. Chem. A* **2017**, 5, 24037.
- [43] C. Wang, Z. Zhang, S. Pejić, R. Li, M. Fukuto, L. Zhu, G. Sauvé, *Macromolecules* **2018**, 51, 9368.
- [44] I. E. Jacobs, Y. Lin, Y. Huang, X. Ren, D. Simatos, C. Chen, D. Tjhe, M. Statz, L. Lai, P. A. Finn, W. G. Neal, G. D'Avino, V. Lemaure, S. Fratini, D. Beljonne, J. Strzalka, C. B. Nielsen, S. Barlow,

- S. R. Marder, I. McCulloch, H. Sirringhaus, *Adv. Mater.* **2021**, 2102988, <https://doi.org/10.1002/adma.202102988>.
- [45] S. Zokaei, D. Kim, E. Järsvall, A. M. Fenton, A. R. Weisen, S. Hultmark, P. H. Nguyen, A. M. Matheson, A. Lund, R. Kroon, M. L. Chabinyk, E. D. Gomez, I. Zozoulenko, C. Müller, *Mater. Horiz.* **2022**, 9, 433.
- [46] V. Coropceanu, J. Cornil, D. A. da Silva Filho, Y. Olivier, R. Silbey, J.-L. Bredas, *Chem. Rev.* **2007**, 107, 926.
- [47] J. M. Moix, M. Khasin, J. Cao, *New J. Phys.* **2013**, 15, 085010.
- [48] D. Balzer, T. J. A. M. Smolders, D. Blyth, S. N. Hood, I. Kassal, *Chem. Sci.* **2021**, 12, 2276.
- [49] R. Coehoorn, W. F. Pasveer, P. A. Bobbert, M. A. J. Michels, *Phys. Rev. B* **2005**, 72, 155206.
- [50] H. C. F. Martens, I. N. Hulea, I. Romijn, H. B. Brom, W. F. Pasveer, M. A. J. Michels, *Phys. Rev. B* **2003**, 67, 121203.
- [51] S. D. Baranovskii, T. Faber, F. Hensel, P. Thomas, *J. Phys.: Condens. Matter* **1997**, 9, 2699.
- [52] J. Cottaar, L. J. A. Koster, R. Coehoorn, P. A. Bobbert, *Phys. Rev. Lett.* **2011**, 107, 136601.
- [53] S. Manjoj Gali, G. D'Avino, P. Aurel, G. Han, Y. Yi, T. A. Papadopoulos, V. Coropceanu, J.-L. Bredas, G. Hadziioannou, C. Zannoni, L. Muccioli, *J. Chem. Phys.* **2017**, 147, 134904.
- [54] H. Bässler, *Advances in Disordered Semiconductors*, World Scientific, Singapore **1990**.
- [55] N. Felekidis, A. Melianas, M. Kemerink, *Org. Electron.* **2018**, 61, 318.
- [56] Z. Liang, H. H. Choi, X. Luo, T. Liu, A. Abtahi, U. S. Ramasamy, J. A. Hitron, K. N. Baustert, J. L. Hempel, A. M. Boehm, A. Ansary, D. R. Strachan, J. Mei, C. Risko, V. Podzorov, K. R. Graham, *Nat. Mater.* **2021**, 20, 518.
- [57] A. R. Chew, R. Ghosh, Z. Shang, F. C. Spano, A. Salleo, *J. Phys. Chem. Lett.* **2017**, 8, 4974.
- [58] P. Y. Yee, D. T. Scholes, B. J. Schwartz, S. H. Tolbert, *J. Phys. Chem. Lett.* **2019**, 10, 4929.
- [59] R. Ghosh, C. K. Luscombe, M. Hamsch, S. C. B. Mannsfeld, A. Salleo, F. C. Spano, *Chem. Mater.* **2019**, 31, 7033.
- [60] M. Upadhyaya, M. Lu-Díaz, S. Samanta, M. Abdullah, K. Dusoe, K. R. Kittilstved, D. Venkataraman, Z. Akšamija, *Adv. Sci.* **2021**, 8, 2101087.
- [61] W. Liu, L. Müller, S. Ma, S. Barlow, S. R. Marder, W. Kowalsky, A. Köhn, R. Lovrincic, *J. Phys. Chem. C* **2018**, 122, 27983.